Flexible ion-conducting membranes with 3D continuous nanohybrid networks for high-performance solid-state metallic lithium batteries

Lehao Liu, Dongmei Zhang, Tianrong Yang, Weihao Hu, Xianglong Meng, Jinshan Mo, Wenyan Hou, Qianxiao Fan, Kai Liu, Bing Jiang, Lihua Chu, Meicheng Li[*]

State Key Laboratory of Alternate Electrical Power System with Renewable Energy Sources, School of New Energy, North China Electric Power University, Beijing 102206, China

A B S T R A C T

Polyethylene oxide (PEO)-based electrolytes are considered as one of the most promising solid-state electrolytes for next-generation lithium batteries with high safety and energy density; however, the drawbacks such as insufficient ion conductance, mechanical strength and electrochemical stability hinder their applications in metallic lithium batteries. To enhance their overall properties, flexible and thin composite polymer electrolyte (CPE) membranes with 3D continuous aramid nanofiber (ANF)–$Li_{1.4}Al_{0.4}Ti_{1.6}(PO_4)_3$ (LATP) nanoparticle hybrid frameworks are facilely prepared by filling PEO–LiTFSI in the 3D nanohybrid scaffolds via a solution infusion way. The construction of the 3D continuous nanohybrid networks can effectively inhibit the PEO crystallization, facilitate the lithium salt dissociation and meanwhile increase the fast-ion transport in the continuous LATP electrolyte phase, and thus greatly improving the ionic conductivity (∼3 times that of the pristine one). With the integration of the 3D continuity and flexibility of the 3D ANF networks and the thermostability of the LATP phase, the CPE membranes also show a wider electrochemical window (∼5.0 V vs. 4.3 V), higher tensile strength (∼4–10 times that of the pristine one) and thermostability, and better lithium dendrite resistance capability. Furthermore, the CPE-based $LiFePO_4$/Li cells exhibit superior cycling stability (133 mAh/g after 100 cycles at 0.3 C) and rate performance (100 mAh/g at 1 C) than the pristine electrolyte-based cell (79 and 29 mAh/g, respectively). This work offers an important CPE design criteria to achieve comprehensively-upgraded solid-state electrolytes for safe and high-energy metal battery applications.

© 2022 Science Press and Dalian Institute of Chemical Physics, Chinese Academy of Sciences. Published by ELSEVIER B.V. and Science Press. All rights reserved.

1. Introduction

Lithium-ion batteries (LIBs) have been widely applied in portable electronics and electric vehicles, because of their comprehensive advantages such as high energy density, long cycling life and low cost [1]. Next-generation batteries with higher energy density and safety are highly demanded especially in the transportation and grid storage fields [2]. Unfortunately, the organic liquid electrolytes in the commercial LIBs easily cause safety issues such as explosion and ignition, owing to the poor thermal, chemical and electrochemical stabilities of the organic solvents, which also induce other problems such as the Li dendrite formation, dissolution of active materials and side reactions [3–5]. It needs to be mentioned that the safety issues become more severe in the LIBs with higher energy density or the battery packs consisting of many cells. The replacement of the organic liquid electrolytes with solid-state electrolytes can not only eliminate the liquid electrolyte-resulted safety issues, but also offer the potential of achieving higher energy density by applying high-voltage cathodes, conversion-type sulfur or oxygen electrodes, or high-capacity Li metal anodes, which would trigger the severe dendrite growth and battery deterioration in the traditional organic liquid electrolytes [6–12]. The LIB assembly processes can also be simplified due to the additional function/role of the solid electrolytes as separators [13,14].

Solid-state electrolytes are generally classified into organic polymer electrolytes and inorganic ceramic electrolytes. Unlike the ceramic electrolytes, polymer electrolytes based on polymer matrices such as polyethylene oxide (PEO) and lithium salts have advantages of simple fabrication, high flexibility, excellent film formation ability, high chemical compatibility with the lithium anodes, small interfacial resistance with the electrodes and low cost, and thus are considered as one of the most promising solid-state electrolytes in next-generation lithium batteries [4,15–20]. Nevertheless, the polymer electrolytes have obvious drawbacks

---

of low room-temperature ionic conductivity (10^{-6}–10^{-8} S/cm), narrow electrochemical window (usually less than 4.0 V), and poor mechanical and thermal stabilities, which are detrimental to the solid-state battery performance [21–25]. Although increasing the working temperature can facilitate the movement ability of both the polymer segments and the ions for higher ionic conductivity, the polymer electrolytes would lose mechanical strength and dimensional stability [22,26]. Thus, it is necessary to improve the comprehensive properties of the polymer electrolytes for better lithium metal battery performance.

A few important strategies have been exploited to improve the properties of the solid polymer electrolytes such as copolymer design, adding plasticizers, and nanoparticle filling. The ionic conductivity can be greatly increased by constructing cross-linking/co-block polymers or adding organic molecules as plasticizers, but it usually induces other problems such as the formation of by-products, incompatibility with the electrode materials, and the deterioration of the mechanical properties and thermostability of the polymer electrolytes [23,27–29]. In comparison, preparing composite polymer electrolytes (CPEs) by dispersing inert ceramic nanoparticles such as TiO_2, Al_2O_3 and SiO_2 into the polymer matrices can increase the ionic conductivity without sacrificing other properties [30–37]. The inert nanofillers with high specific surface areas and strong Lewis acid-base interactions with the electrolyte ion specifies can both facilitate the lithium salt dissociation and inhibit the polymer crystallization, thus increasing the ion conductivity of the polymer electrolytes [27,28,30,38]. Finite element simulations and nuclear magnetic resonance spectrometry also disclose the occurrence of the ion conduction mostly at the ceramic/polymer interface [39–44]. Recent researches find that Li-containing ceramic electrolyte particles (i.e., active nanofillers) such as $Li_{1+x}Al_xTi_{2-x}(PO_4)_3$ (LATP) and $Li_7La_3Zr_2O_{12}$ (LLZO) can furtherly increase the ion conductivity owing to the additional fast-ion pathways in the ceramic electrolyte phases [43,45–48]. However, the ionic conductivity and the mechanical properties cannot be greatly enhanced by the nanoparticle filling method, because of the severe agglomeration and poor dispersity of the high-surface-area nanofillers in the polymer matrices, the failure to form interconnected nano-reinforcement phases, and the short and discontinuous nanofiller/polymer matrix interfaces [21,49–54].

To circumvent the nanoparticle filling-related issues, designing special CPEs by filling the polymer electrolytes in porous ceramic films as 3D scaffolds can greatly improve the ionic conductivity, electrochemical window and thermostability; however, these CPEs are usually thick and non-flexible, and the porous scaffold fabrication processes (e.g., electrospinning [55–58], hydrogel [59,60], aerogel [54] and template methods [61,62]) are complicated and time-consuming and are not suitable for the large-scale applications. Thus, a few researchers have adopted porous polymer scaffolds (e.g., commercial polypropylene separators) to enhance the flexibility and the mechanical strength, but the CPEs with the non-ion-conducting polymer scaffolds exhibit insufficient ionic conductivity and thermal stability [63,64]. In this regard, it is of significance to develop scalable methods to fabricate ideal 3D porous scaffolds (integrating the merits of both the polymer and ceramic scaffolds) for desirable CPEs with high flexibility, ionic conductivity, oxidization potential and thermostability.

In this study, we exploit a facile method to prepare 3D porous nanohybrid films composed of aramid nanofibers (ANFs) and LATP nanoparticles (Fig. 1c) via freeze-drying of the mixture solution of the ANFs and the LATP nanoparticles, and then filling PEO–LiTFSI electrolyte in the 3D ANF–LATP nanohybrid films via solution infusion to obtain 3D ANF–LATP network-supported CPE membranes with high flexibility and low thickness (Fig. 1a). This approach can avoid the disordered distribution of the ANFs and LATP

nanoparticles in the CPEs, which is always related to the commonly-used solution casting and doctor blading methods (Fig. 1b). In contrast, the freeze drying-based method can alleviate the agglomeration of the nanofillers and induce the formation of the 3D continuous ANF–LATP nanohybrid scaffolds. Moreover, the nanohybrid scaffolds can not only combine the 3D continuity and flexibility of the 3D ANF networks, but also integrate the high thermostability and ionic conductivity of the LATP electrolyte phase. Thus, the 3D ANF–LATP nanohybrid scaffold-supported CPE membranes possess greatly-improved ionic conductivity, electrochemical stability, mechanical strength and thermostability, and the interfacial resistance against the lithium dendrites is greatly enhanced. Furthermore, the CPE-based $LiFePO_4$/Li and $LiNi_{0.5}Co_{0.2}Mn_{0.3}O_2$/Li solid-state cells exhibit superior cycling performance than the pristine PEO–LiTFSI electrolyte-based cells. Hence, this work provides a scalable route to obtain desirable CPE membranes with 3D continuous nanohybrid network design for promising all-solid-state lithium metal battery applications.

2. Experimental

2.1. Preparation of the electrolyte membranes

2.00 g long Kevlar 69 microfiber, 0.40 g potassium hydroxide and 200.00 g anhydrous dimethyl sulfoxide (DMSO) were stirred for about 4 weeks at room temperature until the generation of a dark red ANF dispersion [65]. The PEO–LiTFSI electrolyte membrane was prepared by dissolving 1.83 g PEO with a molecular weight of 600,000 and 0.66 g LiTFSI in 50 mL acetonitrile by vigorous stirring at 40 °C for 24 h, putting the PEO/LiTFSI solution in a Teflon plate, and desiccating them at 60 °C in vacuum for 48 h. The $Li_{1.4}Al_{0.4}Ti_{1.6}(PO_4)_3$ (LATP) nanoparticles were prepared by ball-milling a mixture of Li_2CO_3, Al_2O_3, TiO_2 and $(NH_4)_2HPO_4$ in ethanol at 400–600 r/min for 2 h, calcinating them in an alumina crucible at 80 °C for 3 h, 450 °C for 2 h and 900 °C for 4 h, ball-milling the sintered samples in ethanol at 400–600 r/min for 4 h, and then desiccating them in vacuum at 60 °C for 12 h [66]. The ANF/LATP nanoparticle mixture solutions with various LATP weight content (LATP:ANF = 0, 1, and 2) were prepared by adding the LATP nanoparticles in the 5 mL 10 mg/mL ANF/DMSO dispersion (after dilution with DMSO) and then strongly stirring them for 48 h after an ultrasonication for 6 h. The 3D porous ANF–LATP nanohybrid membranes were prepared by coating the ANF/LATP mixture solution on clean glass slides via a 1000 μm-spacing scraper, putting them in deionized water three times and then in an isopropanol/water solution (1:1 in volume) for 12 h for solvent exchange, and freeze-drying them in vacuum for at least 72 h. The ANF–LATP nanohybrid network-supported CPE membranes were fabricated by dripping the PEO/LiTFSI/acetonitrile solution in the porous ANF–LATP membranes, and desiccating them between two glass panels in vacuum at 60 °C for 48 h (The process was repeated twice for sufficient electrolyte filling). The 3D porous ANF–LATP nanohybrid membranes with the weight ratio of LATP to ANF of 0, 1, and 2 were denoted as ANF, ANF–LATP1, and ANF–LATP2, respectively. The CPE membranes with the weight ratio of LATP to ANF of 0, 1, and 2 were labeled as LATP0, LATP1, and LATP2, respectively. The average weight ratios of the ANF framework in LATP0 electrolyte, and the ANF–LATP frameworks in LATP1 and LATP2 electrolytes are around 30%, and 28% and 42%, respectively.

2.2. Materials characterizations

The crystal structure of the LATP nanoparticles and the electrolyte membranes was measured using a Bruker D8 Focus X-ray diffraction (XRD) analyzer (Cu K_α radiation, λ = 0.154 nm). An FEI
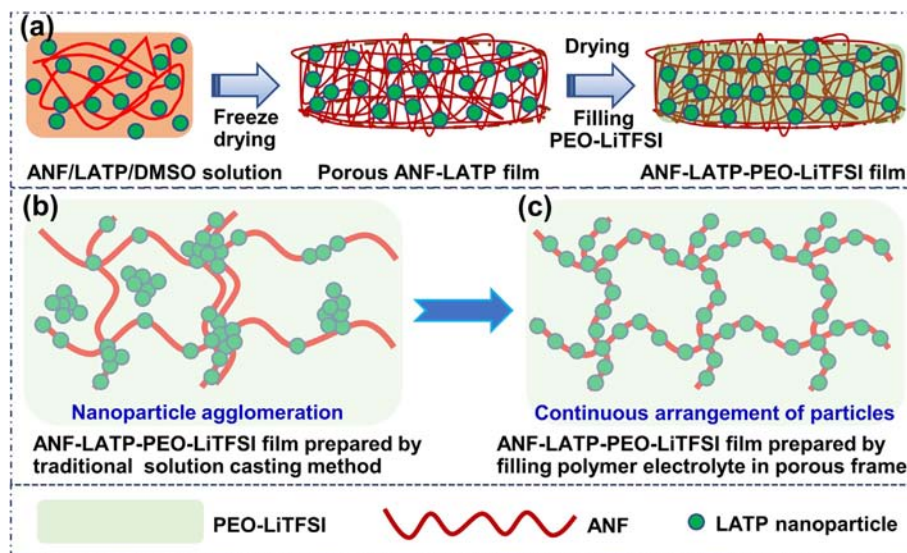
Fig. 1. (a) Schematic description of the preparation process of the ANF–LATP network-supported PEO–LiTFSI electrolyte, and the structure comparison of the ANF–LATP–PEO–LiTFSI electrolytes (b) by the traditional solution casting method and (c) by filling PEO–LiTFSI electrolyte in the porous ANF–LATP nanohybrid framework.

F20 transmission electron microscope (TEM) was utilized to investigate the microstructure of the LATP nanoparticles. The micro-morphology of the ANFs, the LATP nanoparticles and the electrolyte membranes were determined by a Hitachi SU8010 scanning electron microscope (SEM) mounted up an energy dispersive X-ray spectroscopy (EDS). The Frontier Fourier transform infrared (FT-IR) absorbance spectra of the electrolyte membranes were obtained by a PerkinElmer FT-IR spectroscopy analyzer. The mechanical tensile properties of the electrolyte membranes were measured by a GOTECH AI-7000-ST mechanical tester with an ascending velocity of 2 mm/min. A D840TA Q500 thermogravimetric analyzer (TGA) was utilized to detect the thermostability of the electrolyte membranes in argon flow with a heating speed of 10 °C/min. Differential scanning calorimetry (DSC) measurements were taken using a TA Q2000 instrument in nitrogen flow with a temperature range of −90–110 °C and a ramping rate of 5 °C/min. The PEO crystallinity (χ) was calculated based on an equation of $\chi = (\Delta H/F\Delta H_0) \times 100\%$, and ΔH, ΔH_0 and F were the fusion heat of the electrolytes, the melting enthalpy of the completely-crystallized PEO (213.7 J/g), and the weight ratio of PEO in the electrolyte membranes [67].

2.3. Electrochemical measurements

Symmetric stainless steel (SS)/electrolyte/SS cells were assembled for the electrochemical impedance measurements using a Zahner Zennium electrochemical workstation in a frequency range of 10^6–10^{-2} Hz, and the ionic conductivity (σ) of the electrolytes was calculated according to an equation: $\sigma = L/SR$, where L, S and R were the thickness, surface area and resistance of the electrolyte membranes, respectively. Asymmetric SS/electrolyte/Li cells were assembled and then tested in a CHI660E electrochemical workstation by linear sweep voltammetry (LSV) measurements with a scanning rate of 1 mV/s to study the electrochemical stability of the electrolytes. Symmetric Li/electrolyte/Li cells were assembled for investigating the lithium dendrite resistance ability of the electrolyte membranes. To assemble the all-solid-state LiFePO$_4$/electrolyte/Li cells, the LiFePO$_4$ electrodes with ~2.0 mg/cm^2 active loading were firstly prepared by coating a mixture slurry of LiFePO$_4$, polyvinylidene fluoride, carbon black and multi-wall carbon nanotube (8:1:0.97:0.03 in weight) on Al foils followed by vacuum drying at 60 °C for 24 h. The galvanostatic charge and

discharge measurements were taken in a Land LANHE CT2001A system within 2.5–3.8 V at different C rates (1 C = 170 mAh/g). LiNi$_{0.5}$Co$_{0.2}$Mn$_{0.3}$O$_2$/Li cells with an active loading of ~1.5 mg/cm^2 were also assembled with the CPEs and 1 M LiPF$_6$ EC/DMC electrolyte coupled with Celgard polypropylene separators and then electrochemically cycled at various rates (1 C = 180 mAh/g).

3. Results and discussion

3.1. Morphology and microstructure

The LATP electrolyte nanoparticles were prepared through a high-temperature sintering method followed by a ball-milling process. The average size of the LATP nanoparticles was ~61 nm as seen in the TEM images (Fig. 2a), while their average size was ~140 nm as seen in the SEM images (Fig. S1a), which should be attributed to the severe agglomeration of the high-specific-surface-area nanoparticles. The LATP nanoparticles also had typical X-ray diffraction peaks same as LiTi$_2$(PO$_4$)$_3$ crystal (JCPDS card ID: 35-0754, Fig. 2b). The LATP nanoparticles showed a high ionic conductivity of 2.3×10^{-4} S/cm at 25 °C (in the pellet form, Fig. S1b) and high thermal stability of 700 °C (with only 4.0% weight loss before 200 °C because of the water evaporation, Fig. S1c), which are expected to improve the properties of the 3D ANF–LATP network-supported CPE membranes.

The ANFs after the stirring in the DMSO solution have an average diameter of ~10 nm with a high aspect ratio, and these nanofibers are easily interconnected to form 3D networks (Fig. 2c), which would be conducive to the enhancement of the mechanical properties of the ANF-based CPE membranes. The ANF solution mixed with the LATP nanoparticles was then used to prepare the 3D porous ANF–LATP films by coating the solution on glass slides and then freeze-drying in vacuum conditions. The porous ANF films were semi-transparent, but the porous ANF–LATP films became opaque when increasing the LATP content (Fig. S2). All the ANF–LATP films are porous with abundant pores, as can be seen in the surficial and cross-sectional SEM images (Fig. 2d–i). When increasing the weight ratio of LATP to ANF from 0 to 2, the thickness of the porous films decreased (267, 203 and 115 μm for the ANF, ANF–LATP1 and ANF–LATP2 films) due to the high density of the LATP phase (~3.0 g/cm^3), and meanwhile the high-
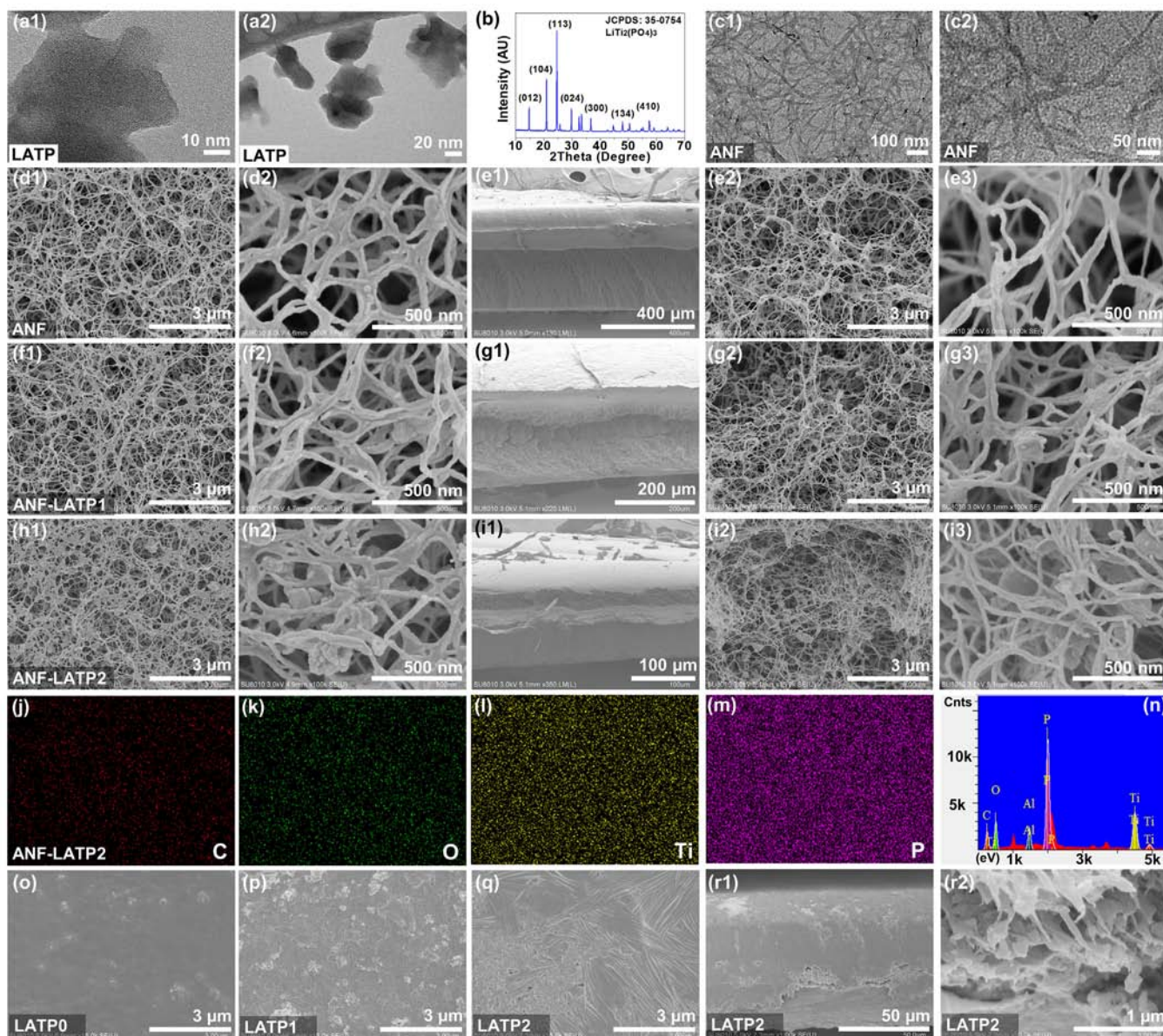
Fig. 2. The microstructures and morphologies of the LATP nanoparticles, ANFs, porous ANF–LATP films and ANF–LATP–PEO–LiTFSI electrolytes. (a1 and a2) TEM images of the LATP nanoparticles; (b) XRD pattern of the LATP nanoparticles; (c1 and c2) TEM images of the ANFs; (d1 and d2) surficial and (e1–e3) cross-sectional SEM images of the porous ANF film; (f1 and f2) surficial and (g1–g3) cross-sectional SEM images of the porous ANF–LATP1 film; (h1 and h2) surficial and (i1–i3) cross-sectional SEM images of the porous ANF–LATP2 film. EDS mapping images of the (j) C, (k) O, (l) Ti and (m) P in Fig. 2(h1), and (n) the corresponding EDS spectra. Surficial SEM images of the (o) LATP0, (p) LATP1 and (q) LATP2 electrolytes, and (r1 and r2) the cross-sectional SEM images of the corresponding LATP2 electrolyte in Fig. 2(q).

conductivity LATP nanoparticles on the ANFs began to connect each other, which would be helpful to increase the ionic conductivity and thermostability of the CPE membranes. The ANFs in the porous ANF and ANF–LATP films remained the interconnected structure, but the diameter of the ANFs increased because of the strong hydrogen bond interactions between the –NH and –C═O groups in the poly(p-phenylene terephthalamide) (PPTA) chains and the merging of the ANFs. The EDS mapping measurements further confirmed the uniform distribution of the LATP nanoparticles in the porous ANF–LATP films (Fig. 2j–n).

The 3D ANF–LATP network-supported CPE membranes were then prepared by filling the PEO–LiTFSI electrolyte in the porous ANF–LATP films (details in the experimental section). As can be seen in the surficial and cross-sectional images of the LATP0 (Fig. 2o and Fig. S3a and b), LATP1 (Fig. 2p and Fig. S3c and d) and LATP2 (Fig. 2q and r) CPE membranes, the pores in the porous

ANF–LATP films were fully filled with the PEO–LiTFSI electrolyte, and the LATP2 CPE membrane had the highest thickness of 58 μm among the CPE films (∼27 and ∼25 μm for the LATP0 and LATP1 films), which should be ascribed to 3D robust (or stiff) ANF–LATP network frames with the high-content LATP phase (ANF:LATP = 1:2 in weight). These thicknesses are much lower than the thickness (usually ≥100 μm) of the electrolyte films prepared by the traditional solution casting method [68,69].

3.2. Electrical, electrochemical, mechanical, and thermal properties

The ionic conductivities of the electrolyte membranes were calculated based on the thickness, surface area and the electrochemical resistance of the electrolyte films. The LATP0 electrolyte displayed a little higher ionic conductivity of 2.0×10^{-6} S/cm than the pristine PEO–LiTFSI electrolyte (1.7×10^{-6} S/cm) at room

temperature (Fig. 3a and Table S1). When incorporated with the LATP nanoparticles into the electrolyte films, the room-temperature ionic conductivities increased to 3.8×10^{-6} and 4.9×10^{-6} S/cm for the LATP1 and LATP2 electrolytes (about three times that of the pristine one), respectively, which should be attributed to the interconnection of the high-ion-conductivity LATP nanoparticles on the ANF networks (Fig. 2f–i) and the enhancement of the ion transport property. When increasing the operation temperature, the ionic conductivity of the electrolytes greatly increased because of the improvement in the mobility of the PEO chains, and the LATP2 electrolyte still showed the highest ionic conductivity of 2.1×10^{-4} S/cm, which is much higher than the pristine PEO–LiTFSI (4.3×10^{-5} S/cm), LATP0 (4.9×10^{-5} S/cm) and LATP1 (1.0×10^{-4} S/cm) electrolytes at 60 °C. When measured at 80 °C, the ionic conductivities were 9.3×10^{-5}, 1.2×10^{-4}, 2.1×10^{-4}, and 4.1×10^{-4} S/cm for the PEO–LiTFSI, LATP0, LATP1, and LATP2 electrolytes, respectively.

To disclose the effect of the ANF–LATP nanohybrid networks on the ionic conductivity of the PEO–LiTFSI electrolyte, X-ray diffraction (XRD), differential scanning calorimetry (DSC) and Fourier transform infrared (FT-IR) measurements were furtherly conducted. The typical X-ray diffraction peaks of 19.1° and 23.4° related to the PEO crystallization appeared in the pristine PEO–LiTFSI electrolyte,

but the peak intensity of the LATP0, LATP1 and LATP2 CPEs greatly decreased (Fig. S4), implying the effective inhibition of the PEO crystallization by the ANF–LATP frameworks. The diffraction peaks of the LATP nanoparticles did not appear in the LATP1 and LATP2 electrolytes, which may be attributed to the low weight content and the uniform distribution of the LATP nanoparticles in the CPE membranes (Fig. 2f–r). The DSC curves showed that the glass transition temperature and the melting point of the electrolytes were around −45 and 51 °C, respectively (Fig. S5). The LATP0 CPE had a PEO crystallinity of 12.6%, which was much lower than the pristine PEO–LiTFSI electrolyte (27.8%) and the LATP1 (24.3%) and LATP2 (23.6%) CPEs (Table S2). In combination with the SEM morphology, XRD and DSC results, we can conclude that the higher ionic conductivity of the LATP0 CPE should be ascribed to the inhibition of the PEO crystallization by the ANF frameworks, while the highest ionic conductivity of the LATP2 CPE should be attributed to not only the reduction of the PEO crystallinity but also the interconnection of the high-loading LATP nanoparticles with high ion conductivity on the ANF networks (i.e., the formation of the ANF–LATP networks for the fast ion transport).

FT-IR measurements were also taken to study the effect of the ANF frameworks on the PEO–LiTFSI electrolyte (Fig. S6). Especially, the intensity of the absorbance peaks at around 739 and 760 cm^{-1}
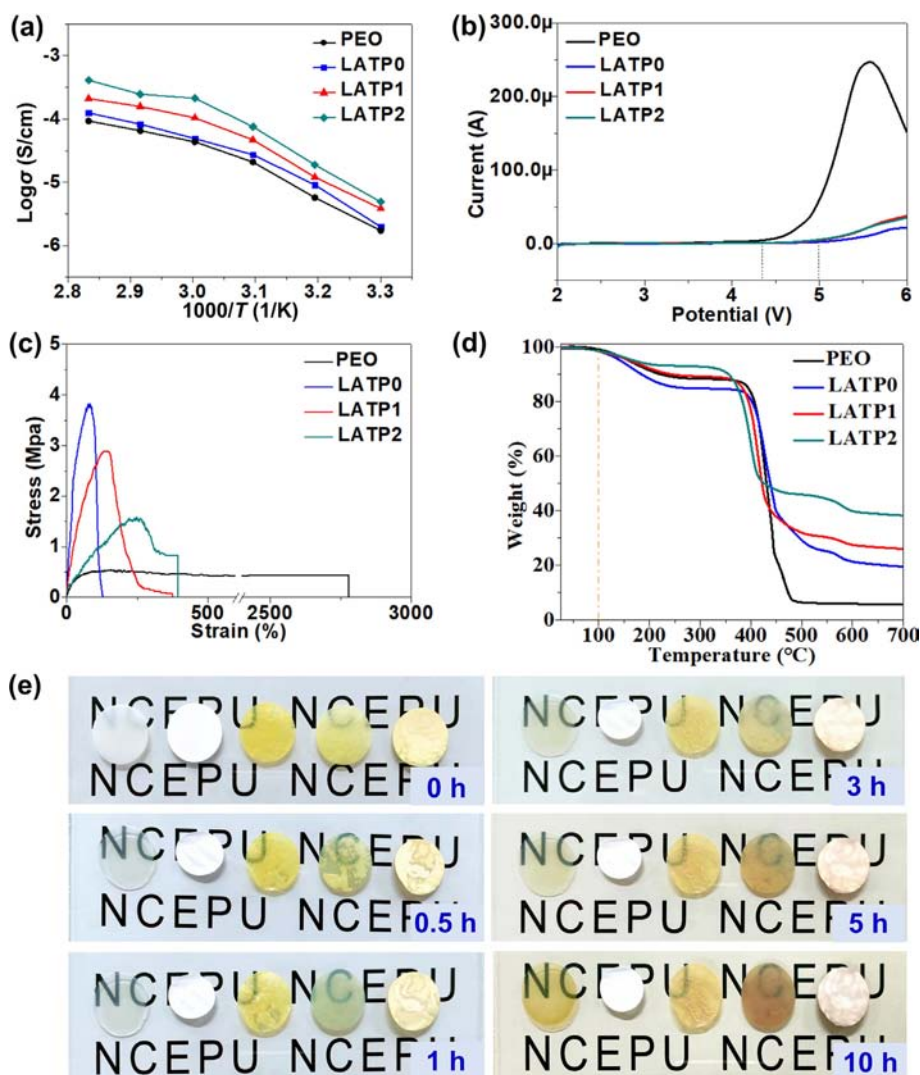

Fig. 3. (a) Ionic conductivity at various temperatures, (b) linear sweep voltammetry profiles, (c) tensile stress–strain curves, (d) TGA curves, and (e) optical photos at 160 °C for 0, 0.5, 1, 3, 5 and 10 h in an oven of the PEO, LATP0, LATP1 and LATP2 membranes (from left to right in Fig. 3e: PEO–LiTFSI, Celgard PP, LATP0, LATP1 and LATP2 membranes).

of the LATP0, LATP1 and LATP2 CPEs were greatly decreased compared to these of the pristine PEO–LiTFSI electrolyte, suggesting that less triflate-containing TFSI⁻ anions were in pairs in the ANF-containing CPEs and the higher LiTFSI dissociation by the hydrogen bond interactions between the –NH groups in the ANFs and the TFSI⁻ anions (mainly the fluorine atoms due to the high electronegativity of the fluorine element and the fluorine-related peak intensity change) [14], which would result in the increase of the free ion concentration and the ionic conductivity of the CPEs [70]. Therefore, the high ionic conductivity of the LATP1 and LATP2 CPEs was ascribed to the formation of the ANF–LATP nanohybrid networks and the resulted increase of the fast-ion transport in the LATP phase, the reduction of the PEO crystallinity, and the facilitation of the lithium salt dissociation.

The electrochemical stability of the electrolytes was then determined by the linear sweep voltammetry (LSV) measurements (Fig. 3b). The pristine PEO–LiTFSI electrolyte had a low oxidation potential of ∼4.3 V at room temperature, while the CPE membranes showed broaden oxidation potentials of ∼5.0 V that is much higher than that of the organic ether-based electrolytes [71]. The practical application of the composite electrolytes in high-voltage $LiNi_{0.5}$-$Co_{0.2}Mn_{0.3}O_2$/Li batteries is further determined in Section 3.4.

The mechanical tensile properties of the electrolyte membranes were also investigated (Fig. 3c). The pristine PEO–LiTFSI electrolyte membrane had a low ultimate tensile strength of 0.4 MPa and a large ultimate tensile strain of 2781%. With the combination of the ANFs, the LATP0 electrolyte membrane had a much higher ultimate tensile strength of 3.8 MPa, which was ∼10 times that of the pristine electrolyte membrane. However, with the addition of the LATP nanoparticles, the ultimate tensile strengths decreased to 2.9 and 1.6 MPa for the LATP1 and LATP2 electrolyte membranes, respectively, and these values were also around 7 and 4 times that of the pristine PEO–LiTFSI electrolyte membrane. The high mechanical strength would be conducive to the inhibition of the lithium dendrite growth [72,73].

The thermostability of the electrolyte membranes was firstly detected by thermal gravimetric analysis (TGA) measurements (Fig. 3d). All the electrolyte membranes had a low weight loss of less than 0.7% before 100 °C, indicating the low solvent content in the solid-state electrolytes. The weight loss at 100–250 °C was related to the decomposition of the lithium salt, and the main decomposition temperature of ∼410 °C was ascribed to the decomposition of PEO. The PEO–LiTFSI, LATP0, LATP1 and LATP2 electrolytes remained 5.5, 19.3, 26.0 and 38.2 wt% at 700 °C, respectively, indicating the high thermal stability of the LATP-containing electrolytes. The thermal stability of the electrolyte membranes was further characterized by observing the shape and melting state of the membranes at 160 °C in an ambient environment (Fig. 3e). The pristine PEO–LiTFSI electrolyte membrane easily melted, and the commercial Celgard polypropene (PP) separator shrank severely after 0.5 h at 160 °C. In stark contrast, the LATP0, LATP1 and LAP2 electrolyte membranes remained their original shape and size without melting even after 10 h at 160 °C, because of the high thermostability of the ANF and LATP-based frameworks. The superior electrical, electrochemical, mechanical and thermal properties of the ANF–LATP network-based CPE membranes would be helpful for prohibiting the nucleation and growth of the lithium dendrites and the destruction of the electrolyte membranes by the lithium dendrites [49,73].

3.3. Interfacial resistance against lithium dendrites

To verify the interfacial resistance capability of the CPE membranes against the lithium dendrites, the Li/electrolyte/Li symmetric cells were assembled and charged-discharged under 0.10 mA/cm² at 60 °C (Fig. 4a–d). The pristine PEO–LiTFSI electrolyte-based cell had an initial overpotential of 0.025 V, but the overpotential suddenly dropped to 0.006 V after 260 h, implying the piercing of the electrolyte membrane by the lithium dendrites and the short circuit of the symmetric cell [43,74]. The subsequent charging and discharging processes with the overpotential flux should be ascribed to the continuous formation of SEI passivation films [75]. In comparison, the LATP0, LATP1 and LATP2 CPE-based cells can stably cycle for 300 h at around 0.040, 0.035 and 0.030 V without the short circuit, respectively, furtherly proving the positive effects of the ANF–LATP frameworks on the mechanical strength and the interfacial resistance ability against the lithium dendrites, in accordance with the mechanical tensile and thermal analysis results (Fig. 3c–e).

The electrochemical impedance spectra before and after the galvanostatic cycling were then investigated (Fig. 4e–h). The pristine PEO–LiTFSI electrolyte-based cell had a small resistance of 134 Ω before the cycling, but the resistance increased to 199 Ω after the galvanostatic cycling. In contrast, the LATP0, LATP1 and LATP2 CPE-based cells exhibited much lower resistances of 177, 153 and 137 Ω after the galvanostatic cycling, respectively, indicating the improvement in the physical contact between the electrolyte membranes and the lithium metal electrodes during the cycling at 60 °C [55,66,76].

SEM images were furtherly taken to disclose the impact of the long-time cycling on the surficial morphology of the electrolyte membranes (Fig. 4i–l). It can be seen clearly that the PEO–LiTFSI electrolyte membrane was covered with many lithium dendrites, and a few cracks were also generated (Fig. 4i), which should be the reason why the PEO–LiTFSI electrolyte-based Li/Li cell had a short circuit phenomenon during the galvanostatic cycling (Fig. 4a). However, there were no obvious dendrites on the LATP1 and LATP2 CPE membranes (Fig. 4k and l), again verifying the dendrite inhibition ability of the ANF–LATP network frameworks [21,77]. SEM characterization on the electrochemically cycled Li electrodes also disclosed that the ANF–LATP frameworks in the composite electrolytes can greatly suppress the lithium dendrite formation on the lithium electrode surface, in stark contrast with the pristine PEO–LiTFSI electrolyte-based Li/Li cells with many dendrites on the Li electrode surface (Fig. S7). These electrochemical measurement results were also consistent with the aforesaid discussion that the excellent thermal stability and high mechanical strength would postpone the lithium dendrite nucleation and prevent the dendrite growth [56,78].

3.4. All-solid-state metallic lithium battery performance

The 3D ANF–LATP nanohybrid framework-based CPE membranes showed comprehensively-enhanced electrical, electrochemical, mechanical and thermal properties and even resistance capability against lithium dendrites as we have discussed in Sections 3.2 and 3.3 (Table S3). To evaluate their implementation in metallic lithium batteries, all-solid-state LiFePO₄/Li batteries were assembled and measured at 60 °C with various charge–discharge rates (Fig. 5a–c and Fig. S8a and b). At such a temperature, the high ionic conductivity of the electrolytes can ensure the normal operation of the battery. The composite electrolyte films should be in quasi-solid-state form above 60 °C according to the DSC measurements (Fig. S5), but the ANF–LATP frameworks would ensure the structural stability of the electrolytes (Fig. 3e). To improve the interfacial contact between the solid-state electrolytes and the electrodes, the all-solid-state cells were kept in an oven at 60 °C for 24 h before the charge–discharge cycling [62,79]. The LATP2 electrolyte-containing cell showed higher discharge capacities of 112, 123, 125, 119 and 100 mAh/g than the cells based on the pristine PEO–LiTFSI (100, 102, 98, 91 and 29 mAh/g), LATP0 (84, 90, 93, 91 and 82 mAh/g) and LATP1 (97, 108, 112, 107 and 95 mAh/g)
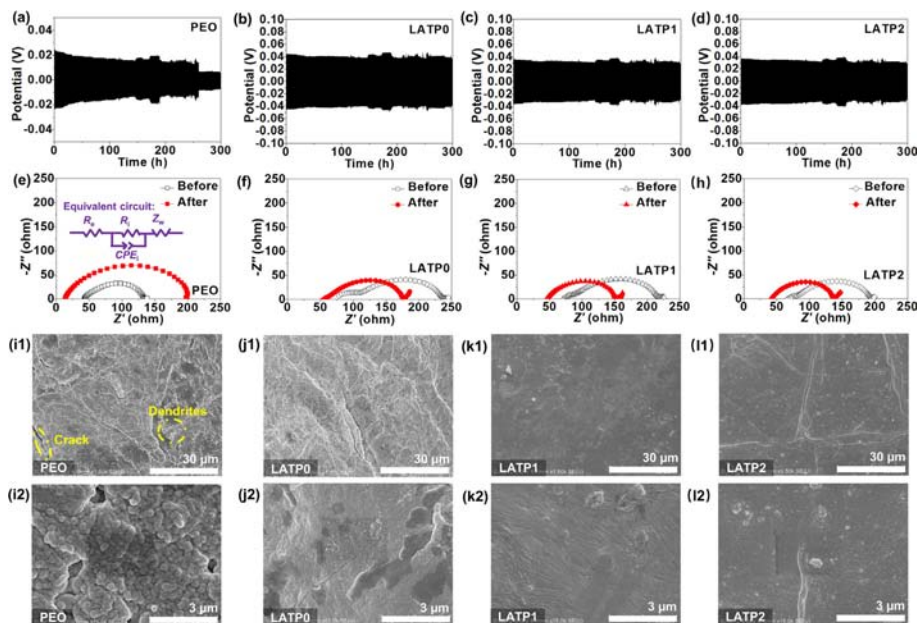
Fig. 4. Galvanostatic cycling curves of the (a) PEO, (b) LATP0, (c) LATP1, (d) LATP2 electrolyte-based Li/Li symmetric cells under 0.10 mA/cm^2 for 300 h at 60 °C. EIS spectra of the Li/Li cells based on the (e) PEO, (f) LATP0, (g) LATP1, (h) LATP2 electrolytes after the Li stripping/plating processes (An equivalent circuit model is given in Fig. 4e). SEM images of the (i) PEO, (j) LATP0, (k) LATP1, (l) LATP2 electrolytes after the stripping/plating processes.
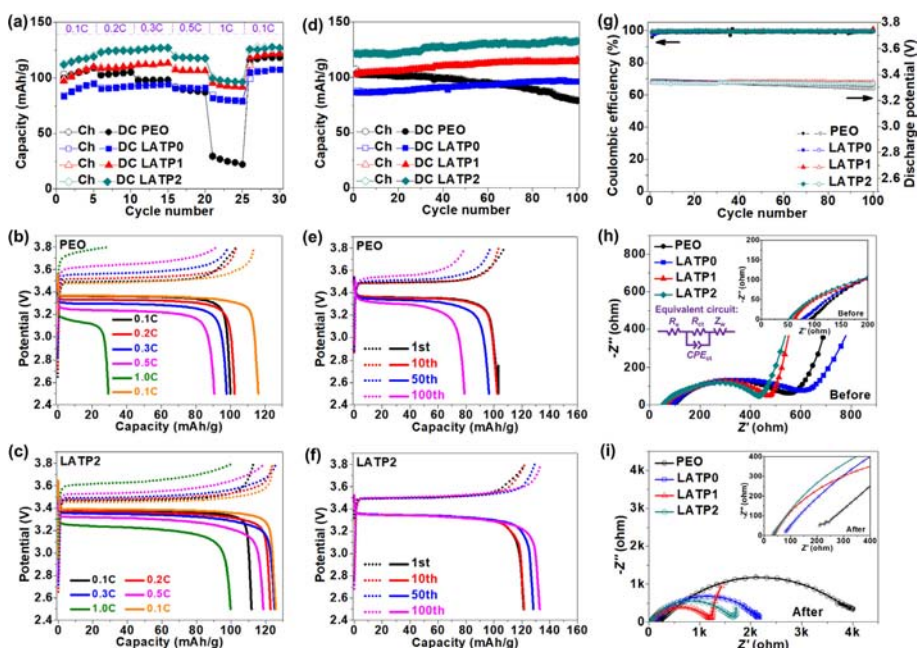

Fig. 5. (a) Rate performance of the solid-state LiFePO$_4$/Li cells at 60 °C, and the corresponding charge–discharge profiles of the (b) PEO and (c) LATP2 electrolyte-based cells at various C rates. (d) Cycling performance of the solid-state cells at 0.3 C and 60 °C, the corresponding charge–discharge profiles of the (e) PEO and (f) LATP2 electrolyte-based cells, and (g) the Coulombic efficiency and discharge potential of the solid-state cells. EIS spectra of the solid-state cells (h) before and (i) after the 100 cycles at 0.3 C and 60 °C.

electrolytes at 0.1, 0.2, 0.3, 0.5 and 1.0 C, respectively. The increase of the capacity at the beginning stage of the charge–discharge processes may be ascribed to the activation of the LiFePO$_4$ electrode [66] and the improvement of the interfacial physical contact between the solid-state electrolytes and the electrodes, which was already confirmed by the decreased resistances of the Li/Li cells in Fig. 4(f–h). When the charge–discharge rate returned to 0.1 C, the LATP2 electrolyte-based cell still exhibited a higher discharge capacity of 126 mAh/g than the PEO–LiTFSI, LATP0 and

LATP1 electrolyte-based cells (116, 105 and 118 mAh/g, respectively).

The long-time cycling stability of the solid-state LiFePO$_4$/Li cells was also investigated (Fig. 5d–f and Fig. S9a and b). The pristine PEO–LiTFSI electrolyte-based cell showed a high discharge capacity of 103 mAh/g at the first cycle, however, the capacity decreased to 79 mAh/g after 100 cycles at 60 °C and 0.3 C with a capacity retention of 77%. In distinct contrast, the LATP2 electrolyte-based cells had much higher capacities of 121 and 133 mAh/g at the first

and 100th cycle than the pristine PEO–LiTFSI, LATP0 (87 and 96 mAh/g) and LATP1 (103 and 116 mAh/g) electrolyte-based cells, respectively. The LATP2 electrolyte-based cell also exhibited superior cycling performance regarding cycling stability and rate performance when compared with other reports (Table S4). Moreover, the pristine PEO–LiTFSI electrolyte-based cell had severe polarization during the cycling (Fig. 5e), however, the CPE-based cells had no obvious polarization (Fig. 5f and Fig. S9a and b). The greatly-improved cycling performance should be ascribed to the ANF–LATP nanohybrid frameworks and the resulted high ionic conductivity, mechanical strength, thermostability and electrochemical stability. It should be mentioned that all the solid-state cells showed higher Coulombic efficiencies of nearly 100% during the whole cycling process than the commercial nonaqueous liquid electrolyte-based cells (Fig. 5g). Moreover, the discharge potentials of all the solid-state cells remained ∼3.3 V after the cycling, again indicating the high cycling stability of the solid-state cells (Fig. 5g).

The electrochemical impedance change of the solid-state cells before and after the long-term cycling was furtherly investigated, and an equivalent circuit was also given (Fig. 5h and i). The semicircle in the high-frequency area and the intersection with the real axis were related to the charge transfer resistance (R_{ct}) and the ohmic resistance (R_e), respectively [14,80]. The LATP2 CPE-based cell showed much lower R_e (54 and 34 Ω) and R_{ct} (382 and 1636 Ω) values than the pristine PEO–LiTFSI electrolyte-based cell (89 and 209 Ω for R_e, and 466 and 3791 Ω for R_{ct}) before and after the long-time cycling at 0.3 C, suggesting the faster charge transport in the LATP2 electrolyte and further proving the positive effect of the ANF–LATP network frame. We can see from Fig. 5(d) that the specific capacity of the LATP0, LAP1 and LATP2-based cells increased in the electrochemical cycling process. The phenomenon of the capacity increase with the cycle number has been also reported in solid-state batteries by other researchers [21,72,81–86], and is usually ascribed to the penetration of the polymer electrolytes in the cathodes and the activation of the electrodes [21,72,79,81,82,85,87,88]. Optimizing the battery preparation process by using soft polymer electrolytes as ionic binders is reported to improve the interface contact for better performance [89,90]. The decrease of the R_e of the CPE-based cells (e.g., 54 to 34 Ω for the LATP2 electrolyte) during the cycling process also verified the improvement of the interfacial contact between the CPE membranes and the electrodes [76]. The long-time activation process in the CPE-based cells may be ascribed to the strong confinement effect of the 3D porous ANF–LATP network frameworks, which could prevent the movement of the high-viscosity PEO–LiTFSI molten phase into the cathodes by capillary action. The thermostability measurements in Fig. 3(e) can verify the confinement effect of the ANF–LATP networks to some extent (The LATP0, LATP1 and LATP2 CPEs remained in their original shape even after 10.0 h at 160 °C, but the pristine PEO–LiTFSI electrolyte easily melted and moved after 0.5 h).

Solid-state LiNi$_{0.5}$Co$_{0.2}$Mn$_{0.3}$O$_2$/Li batteries were also assembled and cycled to investigate the effect of the CPEs operated at high potentials. The organic liquid LiNi$_{0.5}$Co$_{0.2}$Mn$_{0.3}$O$_2$/Li cells had a high initial discharge capacity of 151 mAh/g with a low Coulombic efficiency of 26% within 3.0–4.3 V at 0.1 C and 25 °C, and the liquid electrolyte-containing cells also exhibited high discharge capacities of 140, 129 and 112 mAh/g at 0.2, 0.5 and 1.0 C, respectively (Fig. S10a and b). In comparison, the solid-state LiNi$_{0.5}$Co$_{0.2}$Mn$_{0.3}$O$_2$/Li cells had poor cycling performance when cycled at 0.1–1.0 C within 2.8–4.2 V at 60 °C (Fig. S10c–f), which may be partially ascribed to the lower thermostability of LiNi$_{0.5}$Co$_{0.2}$Mn$_{0.3}$O$_2$ than LiFePO$_4$. This is also why the researchers usually choose LiFePO$_4$ to investigate the solid-state battery performance at 60 °C (Table S4). However, it needs to be mentioned that the LATP2

electrolyte-based LiNi$_{0.5}$Co$_{0.2}$Mn$_{0.3}$O$_2$/Li cell displayed a much higher discharge capacity (127 mAh/g) than the pristine PEO–LiTFSI (90 mAh/g) and LATP0 (95 mAh/g) electrolyte-based cells within 2.8–4.2 V at 0.1 C and 60 °C. When cycled at 0.1 C again, the LATP2 electrolyte-based cell also exhibited a higher discharge capacity (95 mAh/g) than the pristine PEO–LiTFSI (38 mAh/g) and LATP0 (65 mAh/g) electrolyte-based cells, furtherly confirming the positive effect of the ANF–LATP frameworks on the high-voltage batteries.

4. Conclusions

In summary, 3D ANF–LATP nanohybrid network scaffold-supported CPE membranes were fabricated by filling PEO–LiTFSI electrolyte in the 3D porous ANF–LATP membranes. Due to the integration of the 3D continuity and flexibility of the ANF networks and the high thermostability and ion conductivity of the LATP electrolyte phase, and the 3D ANF–LATP nanohybrid network skeleton effect, the CPE membranes exhibited greatly-improved ion conductivity, electrochemical stability, mechanical strength and thermal stability, in sharp contrast with the pristine PEO–LiTFSI electrolyte membrane. The increase of the ionic conductivity was ascribed to the high-conductivity LATP phase on the 3D ANF networks for the fast-ion transport, the suppression of the PEO crystallization, and the facilitation of the lithium salt dissociation. The lithium dendrite inhabitation ability was also enhanced by the 3D ANF–LATP nanohybrid frameworks. Thus, the CPE membrane-containing all-solid-state metallic lithium cells showed better cycling performance than the pristine PEO–LiTFSI electrolyte-based cell. This study provides a novel and effective CPE construction method based on the 3D nanohybrid skeleton design to obtain comprehensively-modified solid-state electrolytes for high-stability solid-state metallic lithium batteries.

Declaration of competing interest

The authors declare that they have no known competing financial interests or personal relationships that could have appeared to influence the work reported in this paper.

Appendix A. Supplementary data

Supplementary data to this article can be found online at https://doi.org/10.1016/j.jechem.2022.08.036.

References

[1] X. Zhang, X. Cheng, Q. Zhang, J. Energy Chem. 25 (2016) 967–984.
[2] L. Liu, M. Li, L. Chu, B. Jiang, R. Lin, X. Zhu, G. Cao, Prog. Mater Sci. 111 (2020) 100655.
[3] Z. Gao, H. Sun, L. Fu, F. Ye, Y. Zhang, W. Luo, Y. Huang, Adv. Mater. 30 (2018) 1–27.

[4] H. Zhang, C. Li, M. Piszcz, E. Coya, T. Rojo, L.M. Rodriguez-Martinez, M. Armand, Z. Zhou, Chem. Soc. Rev. 46 (2017) 797–815.
[5] S. Mu, W. Huang, W. Sun, N. Zhao, M. Jia, Z. Bi, X. Guo, J. Energy Chem. 60 (2021) 162–168.
[6] L. Fan, S. Wei, S. Li, Q. Li, Y. Lu, Adv. Energy Mater. 8 (2018) 1–31.
[7] A. Manthiram, X. Yu, S. Wang, Nat. Rev. Mater. 2 (2017) 1–16.
[8] S. Xin, Y. You, S. Wang, H.C. Gao, Y.X. Yin, Y.G. Guo, ACS Energy Lett. 2 (2017) 1385–1394.
[9] C. Yang, K. Fu, Y. Zhang, E. Hitz, L. Hu, Adv. Mater. 29 (2017) 1–28.
[10] X.-X. Zeng, Y.-X. Yin, N.-W. Li, W.-C. Du, Y.-G. Guo, L.-J. Wan, J. Am. Chem. Soc. 138 (2016) 15825–15828.
[11] L. Chen, W. Li, L.-Z. Fan, C.-W. Nan, Q. Zhang, Adv. Funct. Mater. 29 (2019) 1901047.
[12] X.-B. Cheng, C.-Z. Zhao, Y.-X. Yao, H. Liu, Q. Zhang, Chem 5 (2019) 74–96.
[13] X. Yao, B. Huang, J. Yin, G. Peng, Z. Huang, C. Gao, D. Liu, X. Xu, Chin. Phys. B 25 (2016) 018802.
[14] L. Liu, J. Mo, J. Li, J. Liu, H. Yan, J. Lyu, B. Jiang, L. Chu, M. Li, J. Energy Chem. 48 (2020) 334–343.
[15] Q. Ma, H. Zhang, C. Zhou, L. Zheng, P. Cheng, J. Nie, W. Feng, Y.S. Hu, H. Li, X. Huang, L. Chen, M. Armand, Z. Zhou, Angew. Chem. Int. Ed. 55 (2016) 2521–2525.
[16] R. Chen, W. Qu, X. Guo, L. Li, F. Wu, Mater. Horiz. 3 (2016) 487–516.
[17] L. Chen, Y. Li, S.P. Li, L.Z. Fan, C.W. Nan, J.B. Goodenough, Nano Energy 46 (2018) 176–184.
[18] S.-J. Tan, X.-X. Zeng, Q. Ma, X.-W. Wu, Y.-G. Guo, Electrochem. Energy Rev. 1 (2018) 113–138.
[19] C. Tao, M.H. Gao, B.H. Yin, B. Li, Y.P. Huang, G.W. Xu, J.J. Bao, Electrochim. Acta 257 (2017) 31–39.
[20] J. Mo, D. Zhang, M. Sun, L. Liu, W. Hu, B. Jiang, L. Chu, M. Li, Polymers 13 (2021) 3992.
[21] X.F. Yang, Q. Sun, C.T. Zhao, X.J. Gao, K.R. Adair, Y.L. Liu, J. Luo, X.T. Lin, J.N. Liang, H. Huang, L. Zhang, R. Yang, S.G. Lu, R.Y. Li, X.L. Sun, Nano Energy 61 (2019) 567–575.
[22] T. Watanabe, Y. Inafune, M. Tanaka, Y. Mochizuki, F. Matsumoto, H. Kawakami, J. Power Sources 423 (2019) 255–262.
[23] H. Duan, Y.-X. Yin, X.-X. Zeng, J.-Y. Li, J.-L. Shi, Y. Shi, R. Wen, Y.-G. Guo, L.-J. Wan, Energy Storage Mater. 10 (2018) 85–91.
[24] Z. Cheng, T. Liu, B. Zhao, F. Shen, H. Jin, X. Han, Energy Storage Mater. 34 (2021) 388–416.
[25] P. Ding, Z. Lin, X. Guo, L. Wu, Y. Wang, H. Guo, L. Li, H. Yu, Mater. Today 51 (2021) 449–474.
[26] Y. Zhang, W. Lu, L. Cong, J. Liu, L. Sun, A. Mauger, C.M. Julien, H. Xie, J. Liu, J. Power Sources 420 (2019) 63–72.
[27] W. Liu, N. Liu, J. Sun, P.C. Hsu, Y. Li, H.W. Lee, Y. Cui, Nano Lett. 15 (2015) 2740–2745.
[28] J. Zhang, X. Zang, H. Wen, T. Dong, J. Chai, Y. Li, B. Chen, J. Zhao, S. Dong, J. Ma, L. Yue, Z. Liu, X. Guo, G. Cui, L. Chen, J. Mater. Chem. A 5 (2017) 4940–4948.
[29] J. Hu, W. Wang, B. Zhou, Y. Feng, X. Xie, Z. Xue, J. Membr. Sci. 575 (2019) 200–208.
[30] J. Zhang, N. Zhao, M. Zhang, P.K. Chu, X. Guo, Z. Di, X. Wang, H. Li, Nano Energy 28 (2016) 447–454.
[31] X. Li, D. Wang, H. Wang, H. Yan, Z. Gong, Y. Yang, ACS Appl. Mater. Interfaces 11 (2019) 22745–22753.
[32] Y. Sun, X.W. Zhan, J.Z. Hu, Y.K. Wang, S. Gao, Y.H. Shen, Y.T. Cheng, ACS Appl. Mater. Interfaces 11 (2019) 12467–12475.
[33] C.-Z. Zhao, X.-Q. Zhang, X.-B. Cheng, R. Zhang, R. Xu, P.-Y. Chen, H.-J. Peng, J.-Q. Huang, Q. Zhang, Proc. Natl. Acad. Sci. USA 114 (2017) 11069.
[34] Z. He, L. Chen, B. Zhang, Y. Liu, L.-Z. Fan, J. Power Sources 392 (2018) 232–238.
[35] D. Lin, W. Liu, Y. Liu, H.R. Lee, P.C. Hsu, K. Liu, Y. Cui, Nano Lett. 16 (2016) 459–465.
[36] X. Fu, C. Li, Y. Wang, L.P. Kovatch, L. Scudiero, J. Liu, W. Zhong, ACS Appl. Mater. Interfaces 10 (2018) 4726–4736.
[37] W. Li, S. Zhang, B. Wang, S. Gu, D. Xu, J. Wang, C. Chen, Z. Wen, ACS Appl. Mater. Interfaces 10 (2018) 23874–23882.
[38] X. Guo, W. Peng, Y. Wu, H. Guo, Z. Wang, X. Li, Y. Ke, L. Wu, H. Fu, J. Wang, Sci. China Mater. 64 (2021) 296–306.
[39] H. Xu, P.-H. Chien, J. Shi, Y. Li, N. Wu, Y. Liu, Y.-Y. Hu, J.B. Goodenough, Proc. Natl. Acad. Sci. USA 116 (2019) 18815.
[40] Z.J. Sun, Y.H. Li, S.Y. Zhang, L. Shi, H. Wu, H.T. Bu, S.J. Ding, J. Mater. Chem. A 7 (2019) 11069–11076.
[41] W. Liu, D. Lin, J. Sun, G. Zhou, Y. Cui, ACS Nano 10 (2016) 11407–11413.
[42] W. Liu, S.W. Lee, D. Lin, F. Shi, S. Wang, A.D. Sendek, Y. Cui, Nat. Energy 2 (2017) 1–7.
[43] T. Yang, J. Zheng, Q. Cheng, Y.-Y. Hu, C.K. Chan, ACS Appl. Mater. Interfaces 9 (2017) 21773–21780.
[44] J. Zheng, P. Wang, H. Liu, Y.-Y. Hu, ACS Appl. Energy Mater. 2 (2019) 1452–1459.
[45] J. Cao, L. Wang, X. He, M. Fang, J. Gao, J. Li, L. Deng, H. Chen, G. Tian, J. Wang, S. Fan, J. Mater. Chem. A 1 (2013) 5955.
[46] X. Zhang, N. Li, Z. Hu, J. Yu, Y. Wang, J. Zhu, J. Membr. Sci. 581 (2019) 355–361.
[47] Z. Huang, W. Pang, P. Liang, Z. Jin, N. Grundish, Y. Li, C.-A. Wang, J. Mater. Chem. A 7 (2019) 16425–16436.
[48] Y. Zhao, Z. Huang, S. Chen, B. Chen, J. Yang, Q. Zhang, F. Ding, Y. Chen, X. Xu, Solid State Ionics 295 (2016) 65–71.
[49] W. Tang, S. Tang, C. Zhang, Q. Ma, Q. Xiang, Y.-W. Yang, J. Luo, Adv. Energy Mater. 8 (2018) 1800866.
[50] K.Q. He, C.L. Chen, R. Fan, C. Liu, C.Z. Liao, Y. Xu, J.N. Tang, R.K.Y. Li, Compos. Sci. Technol. 175 (2019) 28–34.
[51] M. Dirican, C. Yan, P. Zhu, X. Zhang, Mater. Sci. Eng. Res. 136 (2019) 27–46.
[52] L. Zhu, P. Zhu, Q. Fang, M. Jing, X. Shen, L. Yang, Electrochim. Acta 292 (2018) 718–726.
[53] S. Gomari, M. Esfandeh, I. Ghasemi, Solid State Ionics 303 (2017) 37–46.
[54] D. Lin, P.Y. Yuen, Y. Liu, W. Liu, N. Liu, R.H. Dauskardt, Y. Cui, Adv. Mater. 30 (2018) 1802661.
[55] K. Fu, Y. Gong, J. Dai, A. Gong, X. Han, Y. Yao, C. Wang, Y. Wang, Y. Chen, C. Yan, Y. Li, E.D. Wachsman, L. Hu, Proc. Natl Acad. Sci. USA 113 (2016) 7094–7099.
[56] H. Zhai, P. Xu, M. Ning, Q. Cheng, J. Mandal, Y. Yang, Nano Lett. 17 (2017) 3182–3187.
[57] D. Li, L. Chen, T. Wang, L.-Z. Fan, ACS Appl. Mater. Interfaces 10 (2018) 7069–7078.
[58] X. Wang, Y. Zhang, X. Zhang, T. Liu, Y.-H. Lin, L. Li, Y. Shen, C.-W. Nan, ACS Appl. Mater. Interfaces 10 (2018) 24791–24798.
[59] J. Bae, Y. Li, J. Zhang, X. Zhou, F. Zhao, Y. Shi, J.B. Goodenough, G. Yu, Angew. Chem. Int. Ed. 57 (2018) 2096–2100.
[60] J. Bae, Y. Li, F. Zhao, X. Zhou, Y. Ding, G. Yu, Energy Storage Mater. 15 (2018) 46–52.
[61] K. Fu, Y. Gong, G.T. Hitz, D.W. McOwen, Y. Li, S. Xu, Y. Wen, L. Zhang, C. Wang, G. Pastel, J. Dai, B. Liu, H. Xie, Y. Yao, E.D. Wachsman, L. Hu, Energy Environ. Sci. 10 (2017) 1568–1575.
[62] X. Wang, H. Zhai, B. Qie, Q. Cheng, A. Li, J. Borovilas, B. Xu, C. Shi, T. Jin, X. Liao, Y. Li, X. He, S. Du, Y. Fu, M. Dontigny, K. Zaghib, Y. Yang, Nano Energy 60 (2019) 205–212.
[63] M. Zhang, A. Gui, W. Sun, J. Becking, O. Riedel, X. He, D. Berghus, V. Siozios, D. Zhou, T. Placke, M. Winter, P. Bieker, J. Electrochem. Soc. 166 (2019) A2142–A2150.
[64] Z.-J. He, L.-Z. Fan, Rare Met. 37 (2018) 488–496.
[65] L. Liu, J. Lyu, J. Mo, H. Yan, L. Xu, P. Peng, J. Li, B. Jiang, L. Chu, M. Li, Nano Energy 69 (2020) 104398.
[66] L. Liu, L. Chu, B. Jiang, M. Li, Solid State Ionics 331 (2019) 89–95.
[67] X. Zhang, J. Xie, F. Shi, D. Lin, Y. Liu, W. Liu, A. Pei, Y. Gong, H. Wang, K. Liu, Y. Xiang, Y. Cui, Nano Lett. 18 (2018) 3829–3838.
[68] X. Yang, K.R. Adair, X. Gao, X. Sun, Energy Environ. Sci. 14 (2021) 643–671.
[69] J. Wu, Z. Rao, Z. Cheng, L. Yuan, Z. Li, Y. Huang, Adv. Energy Mater. 9 (2019) 1902767.
[70] J. Yue, S. Xin, Y.-G. Guo, Curr. Opin. Electrochem. 22 (2020) 195–202.
[71] J. Lopez, Y. Sun, D.G. Mackanic, M. Lee, A.M. Foudeh, M.-S. Song, Y. Cui, Z. Bao, Adv. Mater. 30 (2018) 1804142.
[72] S. Li, J. Lu, Z. Geng, Y. Chen, X. Yu, M. He, H. Li, ACS Appl. Mater. Interfaces 14 (2022) 1195–1202.
[73] N. Meng, F. Lian, G. Cui, Small 17 (2021) 2005762.
[74] X. Ke, Y. Cheng, J. Liu, L. Liu, N. Wang, J. Liu, C. Zhi, Z. Shi, Z. Guo, ACS Appl. Mater. Interfaces 10 (2018) 13552–13561.
[75] L. Chen, L.Z. Fan, Energy Storage Mater. 15 (2018) 37–45.
[76] M. Zhang, P. Pan, Z. Cheng, J. Mao, L. Jiang, C. Ni, S. Park, K. Deng, Y. Hu, K.K. Fu, Nano Lett. 21 (2021) 7070–7078.
[77] L. Yang, D. Luo, Y. Zheng, T. Yang, Q. Ma, Y. Nie, H. Dou, Y. Zhang, R. Huang, A. Yu, L. Shui, X. Wang, Z. Chen, Adv. Funct. Mater. (2022) 2204778.
[78] R. Khurana, J.L. Schaefer, L.A. Archer, G.W. Coates, J. Am. Chem. Soc. 136 (2014) 7395–7402.
[79] S.-H.-S. Cheng, K.-Q. He, Y. Liu, J.-W. Zha, M. Kamruzzaman, R.-L.-W. Ma, Z.-M. Dang, R.K.Y. Li, C.Y. Chung, Electrochim. Acta 253 (2017) 430–438.
[80] O. Sheng, C. Jin, J. Luo, H. Yuan, H. Huang, Y. Gan, J. Zhang, Y. Xia, C. Liang, W. Zhang, X. Tao, Nano Lett. 18 (2018) 3104–3112.
[81] Y. Zhao, Y. Bai, Y. Bai, M. An, G. Chen, W. Li, C. Li, Y. Zhou, J. Power Sources 407 (2018) 23–30.
[82] R. Liu, P. He, Z. Wu, F. Guo, B. Huang, Q. Wang, Z. Huang, C.-A. Wang, Y. Li, J. Electroanal. Chem. 822 (2018) 105–111.
[83] B. Zhang, Y. Zhang, N. Zhang, J. Liu, L. Cong, J. Liu, L. Sun, A. Mauger, C.M. Julien, H. Xie, X. Pan, J. Power Sources 428 (2019) 93–104.
[84] N. Wu, P.-H. Chien, Y. Qian, Y. Li, H. Xu, N.S. Grundish, B. Xu, H. Jin, Y.-Y. Hu, G. Yu, J.B. Goodenough, Angew. Chem. Int. Ed. 59 (2020) 4131–4137.
[85] S.J. Chen, J.Y. Wang, Z.Y. Wei, Z.H. Zhang, Y.H. Deng, X.Y. Yao, X.X. Xu, J. Power Sources 431 (2019) 1–7.
[86] J.Y. Wan, J. Xie, X. Kong, Z. Liu, K. Liu, F.F. Shi, A. Pei, H. Chen, W. Chen, J. Chen, X.K. Zhang, L.Q. Zong, J.Y. Wang, L.Q. Chen, J. Qin, Y. Cui, Nat. Nanotechnol. 14 (2019) 705–711.
[87] Y.-C. Jung, S.-M. Lee, J.-H. Choi, S.S. Jang, D.-W. Kim, J. Electrochem. Soc. 162 (2015) A704–A710.
[88] B. Chen, Z. Huang, X. Chen, Y. Zhao, Q. Xu, P. Long, S. Chen, X. Xu, Electrochim. Acta 210 (2016) 905–914.
[89] Z. Zhang, Y. Zhao, S. Chen, D. Xie, X. Yao, P. Cui, X. Xu, J. Mater. Chem. A 5 (2017) 16984–16993.
[90] C. Wang, Y. Yang, X. Liu, H. Zhong, H. Xu, Z. Xu, H. Shao, F. Ding, ACS Appl. Mater. Interfaces 9 (2017) 13694–13702.